2018

Improved deformation behavior in Ti-Zr-Fe-Mn alloys comprising the C14 type Laves and β phases

Chirag D. Rabadia
Edith Cowan University, c.rabadia@ecu.edu.au

Y. J. Liu

Syed F. Jawed
Edith Cowan University, s.jawed@ecu.edu.au

L. Wang

Y. H. Li

See next page for additional authors

10.1016/j.matdes.2018.10.049
Rabadia, C. D., Liu, Y. J., Jawed, S. F., Wang, L., Li, Y. H., Zhang, X. H., ... & Zhang, L. C. (2018). Improved deformation behavior in Ti-Zr-Fe-Mn alloys comprising the C14 type Laves and β phases. *Materials & Design, 160*. 1059-1070. Available here.

Materials and Design 160 (2018) 1059–1070

Contents lists available at ScienceDirect

Materials and Design

journal homepage: www.elsevier.com/locate/matdes

Improved deformation behavior in Ti-Zr-Fe-Mn alloys comprising the C14 type Laves and β phases

C.D. Rabadia [a], Y.J. Liu [b], S.F. Jawed [a], L. Wang [c,*], Y.H. Li [d], X.H. Zhang [d], T.B. Sercombe [b], H. Sun [a], L.C. Zhang [a,*]

[a] School of Engineering, Edith Cowan University, 270 Joondalup Drive, Joondalup, Perth, WA 6027, Australia
[b] School of Engineering, The University of Western Australia, 35 Stirling Highway, Perth, WA 6009, Australia
[c] State Key Laboratory of Metal Matrix Composites, School of Material Science and Engineering, Shanghai Jiao Tong University, No. 800 Dongchuan Road, Shanghai, 200240, PR China
[d] School of Mechanical Engineering, Xi'an University of Science and Technology, Xi'an 710054, China

HIGHLIGHTS

- The C14 type Laves phase is formed in all the Ti-35Zr-5Fe-xMn alloys.
- Yield strength, hardness and plastic strain are affected by the content of Mn.
- Plastic strain correlates inversely with the size of dimples formed on fractured surfaces.
- Ti-35Zr-5Fe displays impressive elongation (32.5%), ultimate strength (~1.7 GPa) and yield strength (~1.1 GPa).

GRAPHICAL ABSTRACT

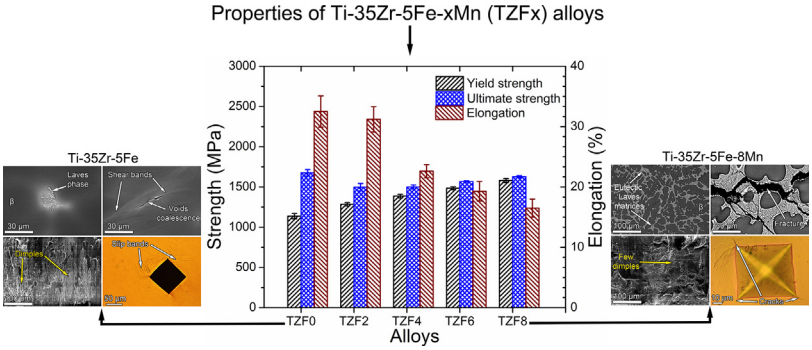

ARTICLE INFO

Article history:
Received 14 September 2018
Received in revised form 23 October 2018
Accepted 31 October 2018
Available online 3 November 2018

Keywords:
Laves phase
Titanium alloy
Deformation
Mechanical strength
Fracture analysis
Shear band

ABSTRACT

Laves phase alloys are promising materials for several structural applications, but the extreme brittleness is the predominant shortcoming of a Laves matrix. One potential solution to overcome this shortcoming is to alloy Laves matrix with some soft matrix. A group of Ti-35Zr-5Fe-xMn (x = 0, 2, 4, 6, 8 wt%) alloys was cast with an aim to improve deformation in Laves alloy compositions. The phase and microstructure analyses reveal dual phase matrices, including a β phase and a C14 type Laves phase in the investigated alloys. The mechanical properties such as yield strength, hardness and plastic strain for the investigated alloys are found to be significantly sensitive to volume fraction of the Laves phase. Ti-35Zr-5Fe shows impressive ultimate compressive strength (~1.7 GPa), yield strength (1138 MPa) and large plastic strain (23.2 %). The fracture mechanisms are dependent on the microstructure of the alloys. Additionally, the work-hardening ability of the investigated alloys have also been evaluated based on the analyses of slip band patterns formed around the micro-hardness indentations. Notably, the extreme brittleness is not encountered in all the Ti-35Zr-5Fe-xMn alloys and all exhibit very good compressive elongation including the maximum (32.5 %) in Ti-35Zr-5Fe.

1. Introduction

AB_2 type Laves phases are well-known for their topologically closed-packed structure among other intermetallic phases [1]. Laves phases have gained much attention in the last 20 years due to their high

* Corresponding authors.
E-mail addresses: wang_liqiang@sjtu.edu.cn (L. Wang), l.zhang@ecu.edu.au, lczhangimr@gmail.com (L.C. Zhang).

https://doi.org/10.1016/j.matdes.2018.10.049

strength at high temperatures, high melting points, low density, excellent hardness as well as their excellent corrosion and oxidation resistances [2,3]. Based on these attracting features, Laves phase alloys are very promising materials for many structural applications [3]. Researchers have recognized >1400 binary and ternary Laves phases until now [4]. Laves phases, which usually form in AB_2 compositions, are categorized into three types: (i) Hexagonal C14 ($MgZn_2$ type structure) (ii) Cubic C15 ($MgCu_2$ type structure) and (iii) Dihexagonal C36 ($MgNi_2$ type structure) [3,5,6]. The larger A atoms and smaller B atoms in AB_2 compositions may be any elements from the Periodic Table and these elements importantly participate in the formation of Laves phases [7]. Interestingly, C15 and C14 types of Laves phases are the second and the fifth most frequently forming intermetallic phases respectively, while C36 type is a less common type of Laves phase [8]. The ideal atomic radii ratio of A and B atoms (R_A/R_B) for Laves phase formation is 1.225; however Laves phase formation generally occurs between R_A/R_B ratio of 1.05 and 1.68. Further, research has also demonstrated that C14 and C36 types of Laves phases have mostly been found between R_A/R_B ratio of 1.12 and 1.26, whereas C15 type has mostly been found between R_A/R_B ratio of 1.1 and 1.35 [9]. The general range of R_A/R_B ratio (i.e. 1.12–1.26) for C14 and C36 types of Laves phases is within the general range of R_A/R_B ratio (i.e. 1.1–1.35) for C15 type Laves phases because the geometric parameter, i.e. R_A/R_B ratio, is not only the one parameter which is responsible for the formation of Laves phase. Several other parameters, such as difference in electronegativities of larger (A) and smaller (B) atoms, number of valence electrons and solubility of individual elements in a base element of an alloy composition, also play a crucial role in the formation of Laves phase [4,10]. Moreover, whilst Laves phases are used in structural applications as a strengthening agent, nonetheless their extreme brittleness and poor fracture toughness are limitations that occur due to their high resistance to dislocation motions. One potential solution to these shortcomings is to alloy Laves particles with a ductile phase matrix [1,4] because the soft ductile phase matrix will have a greater number of slip systems which improve dislocation motions and thereby improve the ductility and fracture toughness [2].

β titanium (Ti) alloys comprising body-centred cubic (bcc) structure, are often the first choice for researchers to overcome the problem of severe brittleness in Laves phase alloys. Alloying of β Ti with Laves matrix [11] can lead Laves phase alloys to exhibit superior plasticity along with high strength, very good fatigue behavior and superior corrosion resistance [12–15]. Therefore, the alloy composition comprising β Ti and Laves matrix can be a very insightful research in the present and future generations of aerospace and automobile applications [16]. Recently, many researchers have studied the mechanical properties of Laves phase alloys which had been alloyed with Ti to improve their ductile behavior [2,11,17].

The selection of elements is a vital phenomenon in designing β Ti alloys because an improved β phase stability can only be achieved using β stabilizing elements [18–20]. Among other β stabilizers, the eutectoid elements such as iron (Fe), manganese (Mn), chromium (Cr) etc. are strong β stabilizers, inexpensive and can improve mechanical and fatigue strength upon addition of even very small quantities in Ti alloys [21,22]. Further, zirconium (Zr) is also a compatible element to Ti because it resides in the same group of the Periodic Table. In addition, Zr possesses excellent corrosion resistance ability and especially high Zr quantities can improve mechanical strength when alloyed with Ti [23]. Hence, the quaternary Ti-Zr-Fe-Mn alloy system has been employed in the present work with an intention of enhancing mechanical and corrosion resistance properties of Laves phase alloys.

The value of R_A/R_B for ternary and quaternary alloys is generally estimated by taking a ratio of average atomic radius of larger elements to average atomic radius of smaller elements present in an alloy composition [2,10,24]. This means that the value of R_A/R_B is dependent only on the geometric parameter (i.e. atomic radius) of the elements present in an alloy composition, but not on the quantities of the alloying elements present in an alloy composition as suggested by Ishimasa et al. [24]. However, the quantities of alloying elements affect the formation of Laves phase based on the solubility of alloying elements in a base element as suggested by Thoma et al. [9]. The metallic atomic radii of Ti, Zr, Fe and Mn are 0.1470, 0.1600, 0.1260 and 0.1270 nm respectively [25]. In Ti-Zr-Fe-Mn system, Ti and Zr are the larger elements, whereas Fe and Mn are the smaller elements. Therefore, the value of R_A/R_B for the Ti-Zr-Fe-Mn system equals to 1.213 which is very much close to 1.225 (i.e. ideal R_A/R_B ratio). Thoma et al. [9] also indicated that C14 type Laves phases are more abundant when the R_A/R_B ratio is close to the ideal R_A/R_B value, whereas C15 type Laves phases are more frequent when the R_A/R_B ratios are above the ideal R_A/R_B value. In addition, the phase diagrams of the Mn—Zr [26] and Mn-Ti-Zr [27] systems suggest the formation of only C14 type Laves phases among the three AB_2 type Laves phases in these systems because C15 and C36 type Laves phases are not likely to form in these phase diagrams. The phase diagrams of Mn—Zr [26], Mn-Ti-Zr [27] and Ti-Zr-Fe [28] systems also indicate a high possibility of C14 type Laves phase formation for the quantity of Zr in between around 25 wt% and 40 wt% in these systems. Research has also shown that small quantities (<10 wt%) of eutectoid elements such as Fe, Cr, Mn etc. are also enough to form Laves phase in Ti—Zr alloys [2,10]. Therefore, in the present work, the quantities of Zr and Fe have been selected as 35 wt% and 5 wt% respectively and the quantity of Mn has been varied from 0 to 8 wt%. The quantities of alloying elements have been selected and a possibility for the formation of C14 type phase in the Ti-Zr-Fe-Mn alloys has been checked, based on the relevant binary and ternary phase diagrams (discussed above) [29] because Ti-Zr-Fe-Mn system alloys have not been investigated much until now.

The points discussed above indicate that there is a high possibility of getting C14 type Laves phase in the Ti-Zr-Fe-Mn system. Moreover, literature on investigations of the Ti-Zr-Fe-Mn system is quite limited, where the present work aims to examine the microstructure, mechanical properties, fracture and elasto-plastic deformation behaviors of the Ti-Zr-Fe-Mn system alloys. The Ti-35Zr-5Fe-xMn (0, 2, 4, 6 and 8 wt%) alloys were designed with an objective to achieve Laves phase in these designed alloys. Furthermore, the concentration of Mn has been varied from 0 to 8 wt% in the Ti-35Zr-5Fe-xMn alloys and the effects of Mn concentration on the Laves phase formation and on the mechanical and fracture properties have been evaluated.

2. Materials and methods

The Ti-35Zr-5Fe-xMn ($x = 0, 2, 4, 6, 8$ wt%) alloys were fabricated from 99.9 % pure alloying elements using a cold crucible levitation melting method. The cast ingot of each alloy was re-melted and flipped five times to ensure the chemical homogeneity in the produced alloys and then rapid quenching of each alloy was employed in a water-cooled copper crucible. Multiple cylindrical rods of all the as-cast Ti-35Zr-5Fe-xMn alloys were first prepared with approximately 4.6 mm diameter from the respective ingot of each alloy using a wire electrical discharge machining. The cylindrical rods of all the produced alloys were then cut using a Buehler Isomet 1000. Note that the abbreviations in the form of TZFx were henceforth used to describe all the as-cast Ti-35Zr-5Fe-xMn alloys; e.g. the abbreviation TZF0 was used to describe Ti-35Zr-5Fe, the abbreviation TZF2 was used to describe Ti-35Zr-5Fe-2Mn and likewise abbreviations were used for the remaining as-cast alloys.

The samples of each alloy were ground using silicon carbide papers for the phase and microstructure analyses. The samples of each alloy were then polished using a Struers MD-Chem polishing cloth with a presence of Struers OP-S colloidal silica suspension for the microstructure analyses. The standard metallographic sample preparation methods were used for preparing samples of all the as-cast alloys. Scanning electron microscopy (SEM) was performed using a high-resolution FEI Verios XHR 460 for the microstructural analyses. Energy dispersive

X-ray spectroscopy (EDX) point analyses and EDX elemental mapping were carried out using an Oxford Instruments X-Max SDD detector equipped with FEI Verios XHR 460.

X-ray diffraction (XRD) was performed on a ground sample of each alloy at room temperature using a PANalytical EMPYREAN X-ray diffractometer. The source of Co Kα with a wavelength of 0.1789 nm, accelerating voltage of 40 kV and emission current of 40 mA were used in an X-ray diffractometer. The XRD tests were carried out over the 2θ angles between 30° and 110° at a scan speed of 0.016°/s and a step size of 0.013°. Phase and structural information of all the as-cast alloys were obtained from the relevant JCPDS files. Volume fractions (V_f) of the phases present in the as-cast alloys were estimated using two methods: (i) The areas for consitutent phases in the microstructure images analyzed by ImageJ software [2,22] (ii) Integrated areas of the XRD diffraction peaks corresponding to the phases present [18,19]. The integrated areas of the diffraction peaks were obtained using a peak fitting program of Origin software with a Pearson VII function [30]. The volume fractions of the β ($V_{f,\beta}$) and C14 ($V_{f,C14}$) phases from the integrated areas of the diffraction peaks were estimated using Eq. (1) and Eq. (2) respectively [18,19,31].

$$V_{f,\beta} = \frac{A_\beta}{A_{C14} + A_\beta} \quad (1)$$

$$V_{f,C14} = \frac{A_{C14}}{A_{C14} + A_\beta} \quad (2)$$

where $V_{f,\beta}$ and $V_{f,C14}$ are the volume fractions and A_β and A_{C14} are the total integrated areas (including all the peaks), corresponding to β and C14 phases respectively.

Uniaxial compression and micro-hardness testing were performed to evaluate the several mechanical properties of the as-cast alloys. The uniaxial compression tests were carried out at room temperature on three cylindrical samples (prepared according to ASTM E9 with approximate length to diameter ratio of 1.8) at a crosshead speed of 0.1 mm/min using an Instron 5982. The average values of yield strength at 0.2 % strain offset ($\sigma_{0.2}$), ultimate compressive strength (σ_{max}) and plastic strain were considered. Vickers micro-hardness tests were performed on a polished sample of each alloy using a Zwick Roell ZHU operated at 5 kgf load and 30 s dwell time. The average values of fifteen indentations were considered for all the as-cast alloys.

Fracture morphologies of the failed samples were obtained using a FEI Verios XHR 460 scanning electron microscope for analyzing the fracture and deformation behaviors of the as-cast alloys. Optical microscopy was carried out using a Zeiss Axiocam to analyze the deformation patterns around the micro-hardness indentations of the as-cast alloys.

3. Results and discussion

3.1. Phase and microstructure analyses

The XRD profiles of the Ti-35Zr-5Fe-xMn alloys are shown in Fig. 1. The dual phase profiles including bcc β (Space group: *Im*-3*m*, Pearson symbol: *cI*2) and hexagonal closed-packed (hcp) C14 type Laves (Space group: $P6_3/mmc$, Pearson symbol: *hP*12) phases are found by matching the diffraction peaks with JCPDS files for all the as-cast alloys. The XRD peaks for Laves phases always match with the XRD peaks of their respective prototype structures, i.e. $MgZn_2$ for C14, $MgCu_2$ for C15, $MgNi_2$ for C36 type Laves phases. This phenomenon can be observed in Fig. 1 as all the peaks other than those found for the β phase in all the investigated alloys match with the standard PDF card of hcp $MgZn_2$ (PDF# 01-071-9623). The identical XRD results for a C14 phase was reported in the literature [11,32,33]. The shift of diffraction peaks toward higher diffraction angles in the XRD profiles of all the Ti-35Zr-5Fe-xMn alloys are evident because of the existence of the low atomic radius elements (Fe and or Mn) in the alloy compositions, e.g. Fe in

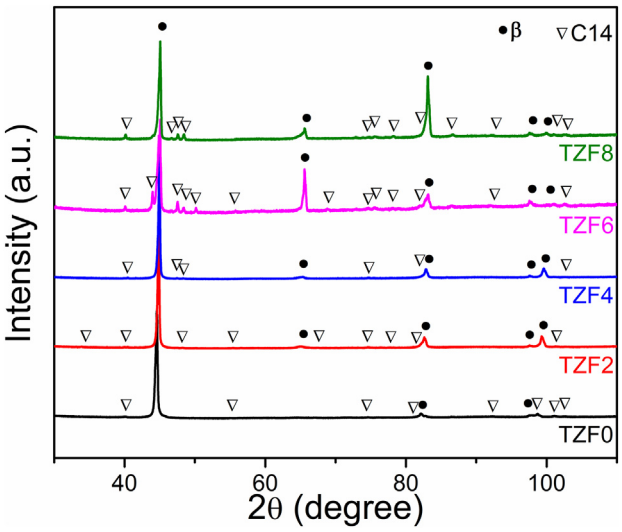

Fig. 1. The XRD profiles of the Ti-35Zr-5Fe-xMn alloys. Note that all the Ti-35Zr-5Fe-xMn alloys are labelled in the forms of TZFx.

TZF0 and both Fe and Mn in the remaining alloys. The values of $V_{f,\beta}$ and $V_{f,C14}$ were estimated based on the integrated areas of the peaks using Eq. (1) and Eq. (2) respectively and the corresponding values of V_f for all the investigated are presented in Table 1. It can be observed in Table 1 that $V_{f,C14}{}^*$ increases as the concentration of Mn increases from 0 to 8 wt%. As a result, TZF8 has the highest amount of $V_{f,C14}{}^*$ and TZF0 has the lowest amount of $V_{f,C14}{}^*$.

Fig. 2 illustrates the microstructure images taken using backscattered SEM for the investigated alloys. The near equiaxed morphologies of β phase and the precipitations of Laves phase are found in the microstructures of all the Ti-35Zr-5Fe-xMn alloys. The morphologies of β phase and Laves phase (white second phase) are shown in Fig. 2 for all the investigated alloys. The precipitation of Laves phase usually occurs due to the segregation of at least two elements [34–36]. The segregation of specific elements in the microstructure depends on the solubility of alloying elements in a base element [37,38]. The rod-shaped Laves phase can be seen in the TZF0 alloy (Fig. 2a inset), whereas the eutectic Laves matrices can be seen in the alloys comprising Mn concentration, i.e. TZF2, TZF4, TZF6 and TZF8 (Fig. 2b–e insets). It has been demonstrated that rod-shaped Laves phase mostly precipitates with relatively low volume fraction in the alloys comprising relatively low quantities of eutectoid elements, whereas the Laves phase with eutectic morphologies precipitates mostly with relatively high volume fraction in the alloys comprising relatively high quantities of eutectoid elements [2]. Therefore, rod-shaped morphologies (with relatively less amount) are found in TZF0 due to comprising only Fe concentration, whereas eutectic morphologies (with relatively high amount) are found in TZF2, TZF4, TZF6 and TZF8 due to comprising the concentrations of Fe and Mn. The precipitations of the Laves phase in this work are mostly found along the grain boundaries because grain boundaries are a kind of crystal defects and preferred sites for the precipitation of second phase particles [39]. Consequently, the precipitation of the Laves phase occurs along the grain boundaries due to diffusion process [40]. The identical rod-shaped and eutectic morphologies of a C14 type Laves phase were reported by many researchers [41–43]. It has been also noted that a very little amount of Laves phase is obtained in TZF0 as compared to other investigated alloys. Consequently, a less number of evident peaks for the C14 phase are obtained in the XRD profile of TZF0 because the XRD technique mostly recognize all the peaks corresponding to the phase with a certain high amount [44]. Furthermore, the faded bright regions are found around the Laves phase as well as at some other places in the microstructures of the TZF0, TZF2, TZF4 and TZF6 alloys. These faded bright regions may be a segregation of a

Table 1
The phase constituents, V_f of the specific phases and the values of lamellar spacing and grain size for the Ti-35Zr-5Fe-xMn alloys. Note that all the Ti-35Zr-5Fe-xMn alloys are labelled in the forms of TZFx.

Alloys	Phases	The results of V_f estimated based on the integrated areas of the XRD peaks		The results of V_f estimated from the microstructure images.		Lamellar spacing (nm)	Grain size (μm)
		$V_{f,\ \beta^*}$ (%)	$V_{f,\ C14^*}$ (%)	$V_{f,\ \beta^{**}}$ (%)	$V_{f,\ C14^{**}}$ (%)		
TZF0	β, C14	99.2	0.8	99.6	0.4	–	135 ± 33
TZF2	β, C14	98.8	1.2	99.1	0.9	340 ± 101	74 ± 13
TZF4	β, C14	97.3	2.7	97.4	2.6	570 ± 154	65 ± 20
TZF6	β, C14	90.3	9.7	93.0	7.0	877 ± 291	49 ± 18
TZF8	β, C14	76.4	23.6	80.6	19.4	1091 ± 508	18 ± 7

specific element present in the alloy compositions. It is confirmed based on the XRD results that the second phase in the investigated alloys is a C14 type Laves phase. However, the details about the exact type of the precipitated Laves phase and the faded bright regions can be attained based on the EDX point analyses and elemental mapping.

The values of $V_{f,\ \beta}$ and $V_{f,\ C14}$ were also estimated from the microstructure images for all the Ti-35Zr-5Fe-xMn alloys using ImageJ software and the same values are presented in Table 1. The values of $V_{f,\ C14}$ estimated using both the techniques (discussed earlier) increase as the concentration of Mn increases because the growth of Laves phase precipitation depends on the solubility of alloying elements in an alloy composition as discussed earlier. This phenomenon indicates that the solubility of Mn becomes poor as the concentration of Mn increases in the Ti-35Zr-5Fe-xMn alloys.

It can also be observed that there is a less difference in the values of $V_{f,\ \beta}$ and $V_{f,\ C14}$ estimated using both the techniques for the TZF0, TZF2 and TZF4 alloys. On the other hand, for the TZF6 and TZF8 alloys, the values of $V_{f,\ C14}{}^{*}$ estimated from the integrated area of the XRD peaks are greater than the corresponding values of $V_{f,\ C14}{}^{**}$ estimated from the microstructure images using ImageJ software (Table 1) because the values of V_f estimated from the microstructure images depend on the selected microstructural region of the analyzed alloys. In the present work, the values of V_f obtained from the microstructure images are used from now onwards in the succeeding explanations.

In addition, lamellar spacing present in the eutectic Laves matrices for the alloys comprising Mn content and grain sizes for all the Ti-35Zr-5Fe-xMn alloys were measured using ImageJ software. The measured values of lamellar spacing and grain size for all the Ti-35Zr-5Fe-

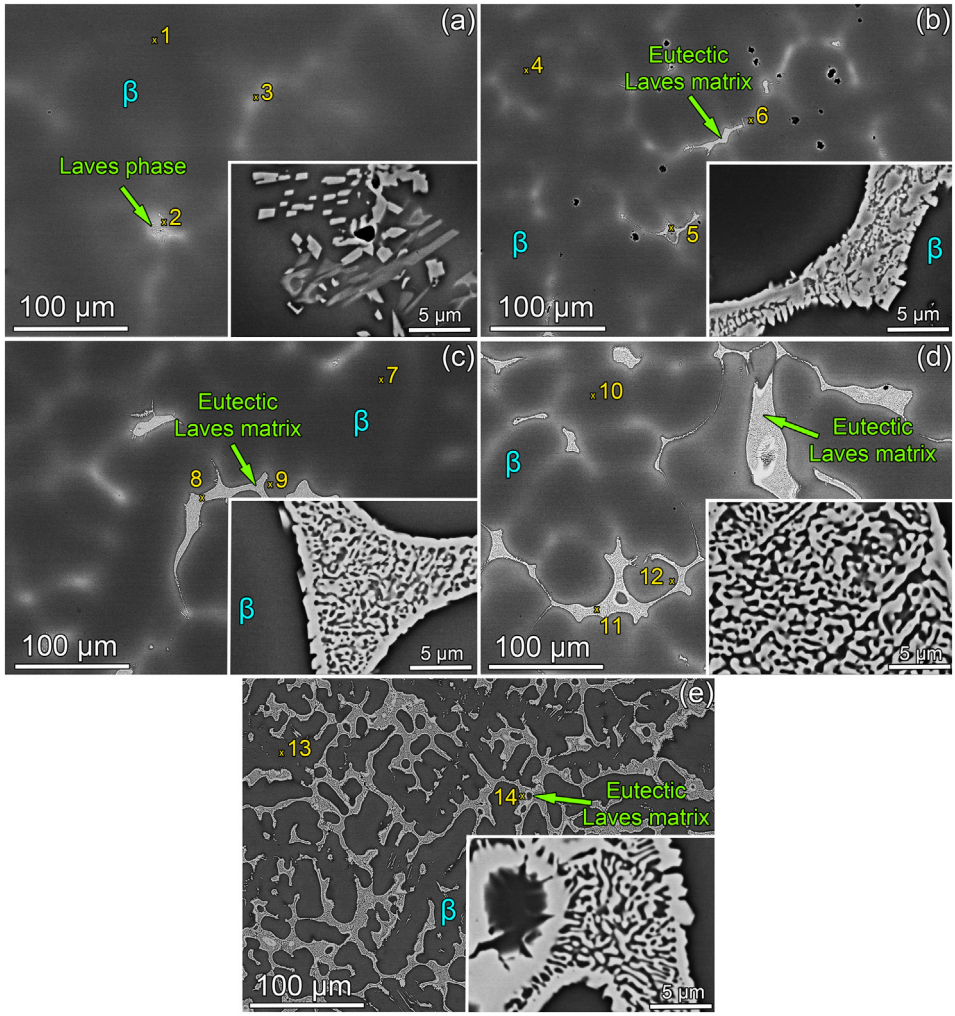

Fig. 2. The microstructure (backscattered SEM) images of (a) TZF0, (b) TZF2, (c) TZF4, (d) TZF6 and (e) TZF8. Note that all the Ti-35Zr-5Fe-xMn alloys are labelled in the forms of TZFx.

Table 2
Chemical compositions of the as-cast alloys and the results of the EDX point analyses carried out on the points marked in Fig. 2. Note that all the Ti-35Zr-5Fe-xMn alloys are labelled in the forms of TZFx.

Alloys	Chemical compositions (wt%)	Points marked in Fig. 2	The quantities of elements obtained from the EDX point analyses			
			Ti (wt%)	Zr (wt%)	Fe (wt%)	Mn (wt%)
TZF0	Ti-35Zr-5Fe	1	67.1	27.3	5.6	–
		2	36.7	37.8	25.5	–
		3	59.8	34.4	5.8	–
TZF2	Ti-35Zr-5Fe-2Mn	4	61.2	32.0	4.7	2.1
		5	40.7	39.8	15.7	3.8
		6	56.2	36.8	4.8	2.2
TZF4	Ti-35Zr-5Fe-4Mn	7	64.0	27.1	4.8	4.1
		8	42.6	34.4	14.8	8.2
		9	59.2	33.1	4.3	3.4
TZF6	Ti-35Zr-5Fe-6Mn	10	61.1	28.8	4.4	5.7
		11	37.0	37.1	13.4	12.5
		12	59.4	31.8	3.8	5.0
TZF8	Ti-35Zr-5Fe-8Mn	13	60.5	28.1	4.2	7.2
		14	35.1	34.2	12.9	17.8

xMn alloys are also summarized in Table 1. In the Ti-35Zr-5Fe-xMn alloys, the values of grain size decrease as the concentration of Mn increases because Fe and Mn elements are the solute elements in the Ti-35Zr-5Fe-xMn alloys and the increase in the quantities of solute elements reduces the grain size; however, the concentration of Mn has only been varied from 0 to 8 wt% in the present work [45]. Therefore, the grain refinement occurs subsequently in the Ti-35Zr-5Fe-xMn alloys as the concentration of Mn increases [45]. In contrast, the values of lamellar spacing increase as the concentration of Mn increases from 2 to 8 wt% in the alloys comprising Mn content because the quantity of solute particles is also one of the factors which controls the lamellar spacing in eutectic matrix [46]. Hence, TZF8 exhibits the maximum lamellar spacing (1091 ± 508 nm) in the eutectic matrices and the lowest grain size (18 ± 7 μm) among the other alloys analyzed in the present work.

EDX point analysis technique is used in the present work to confirm the quantities of the alloying elements (Ti, Zr, Fe and Mn) over the three regions: (i) β phase, (ii) Laves phase and (iii) faded bright regions. In Fig. 2, the points 1, 4, 7, 10 and 13 are marked on the β phase regions, the points 2, 5, 8, 11 and 14 are marked on the Laves phase regions and the points 3, 6, 9 and 12 are marked on the faded bright regions. The EDX point analyses were carried out over all the points marked using a yellow colored cross (x) sign in Fig. 2. As the faded bright regions are not found in TZF8, the corresponding point for the faded bright region is not marked in Fig. 2e. Table 2 summarizes the results of the EDX point analyses carried out on the points marked in Fig. 2. The quantity of Fe in TZF0 and the quantities of Fe and Mn in the alloys comprising Mn content, over the Laves phase morphologies (Points 2, 5, 8, 11 and 14), are obtained more than doubled than their respective nominal quantities, whereas the quantities of Zr, over the Laves phase morphologies, are found close to or slightly greater than their nominal quantities. The quantity of Fe in TZF0 and the quantities of Fe and Mn in the alloys comprises Mn content, over the β phase regions (Points 1, 4, 7, 10 and 13) are obtained close to their respective nominal quantities, whereas the quantities of Zr over the β phase regions are obtained less than their nominal quantities. The quantities of Zr over the faded bright regions (Points 3, 6, 9 and 12) are found in between the quantities of Zr obtained over the β phase and Laves phase regions.

EDX elemental mapping was carried out to obtain the information about the elemental segregations for all the Ti-35Zr-5Fe-xMn alloys. Fig. 3 displays the results of EDX elemental mapping obtained for the TZF0 and TZF8 alloys on their respective backscattered SEM images. In Fig. 3a, the segregations of Fe and Zr are found on the Laves phase morphologies shown in the respective backscattered SEM image of TZF0, whereas the quantity of Ti is almost concentrated over the β phase. Interestingly, the segregation of Zr over the faded bright region can be

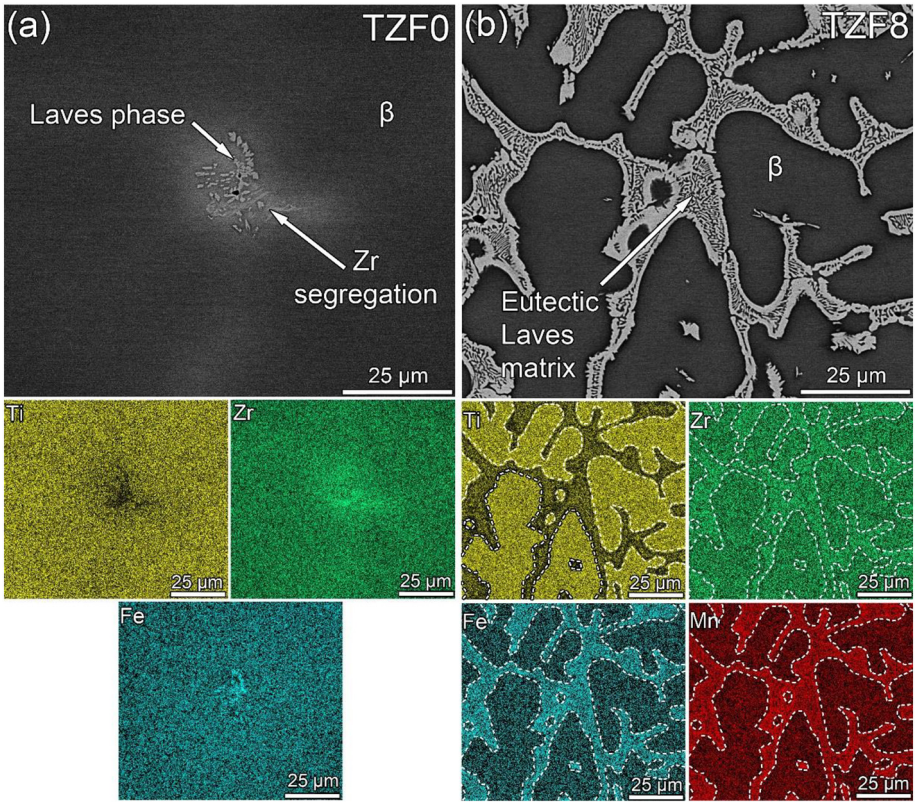

Fig. 3. The results of EDX elemental mapping carried out for (a) TZF0 and (b) TZF8 on their respective backscattered SEM images. Note that the Ti-35Zr-5Fe and Ti-35Zr-5Fe-8Mn alloys are labelled in the forms of TZFx.

seen in the elemental mapping image of Zr (light colored area) in Fig. 3a. This means that the faded bright regions found in the microstructure of the TZF0, TZF2, TZF4 and TZF6 alloys are the segregation of Zr. In Fig. 3b, the segregations of Zr, Fe and Mn are found over the eutectic Laves phase morphologies of TZF8 and Ti is almost concentrated over the β phase in a same way as concentrated in TZF0. The Laves phase morphologies in the elemental mapping images of individual elements (Ti, Zr, Fe and Mn) are shown using white-dashed line in Fig. 3b to clearly depict the regions of the Eutectic Laves matrices. The similar segregation results of Zr, Fe and Mn elements over the Laves phase are found in the TZF2, TZF4 and TZF6 alloys and the segregations of Zr over the faded bright regions are also found in TZF2, TZF4 and TZF6 alloys. Therefore, the EDX elemental mapping results of only TZF0 and TZF8 are presented in the present work. The results of EDX point analyses and elemental mapping infer the Fe_2Zr phase in TZF0 and the $Zr(Fe, Mn)_2$ phase in TZF2, TZF4, TZF6 and TZF8. This means that the quantities of eutectoid elements (i.e. Fe and Mn in the present work) are very much sensitive to the formation of Laves phase along with the quantity of Zr above 30 wt% and the balance quantity of Ti [2].

3.2. Mechanical properties

Fig. 4 shows the engineering stress vs. strain curves obtained for the Ti-35Zr-5Fe-xMn alloys from uniaxial compressive testing. It is detected based on the results displayed in Fig. 4 that none of the Ti-35Zr-5Fe-xMn alloys fail within the elastic limit. Moreover, all the Ti-35Zr-5Fe-xMn alloys exhibit some level of plastic deformation, therefore the issue of extreme embrittlement has not been encountered in the present work. It is noticeable that the compressive elongation values in the present work decrease from the maximum value of 32.5 ± 2.6 % (for TZF0) to the minimum value of 16.5 ± 1.5 % (for TZF8) as the content of Mn and $V_{f,\,C14}$ increase. It is also worth noting from Fig. 4 that the work-hardening ability of the investigated alloys reduces as the difference between σ_{max} and $\sigma_{0.2}$ reduces due to rise in the values of $V_{f,\,C14}$ [47]. Moreover, the value of σ_{max} is influenced by a type of a Laves phase, morphology of the Laves phase and the corresponding V_f of the Laves phase. Hence, the TZF0 alloy exhibits the highest σ_{max} value (1675 ± 41 MPa) among all the investigated alloys because it comprises a rod-shaped Fe_2Zr phase [2]. On the other hand, the value of σ_{max} increases as the V_f of the eutectic matrices (i.e. $Zr(Fe, Mn)_2$ phase) increases in terms of $V_{f,\,C14}$ in the alloys comprising the concentration of Mn.

Fig. 5 depicts the correlation between the values of $\sigma_{0.2}$ and hardness for all the Ti-35Zr-5Fe-xMn alloys. The values of $\sigma_{0.2}$ and hardness

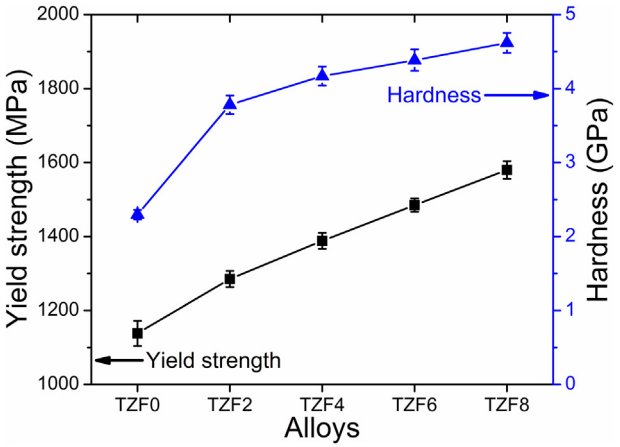

Fig. 5. Yield strength and hardness of the Ti-35Zr-5Fe-xMn alloys. Note that all the Ti-35Zr-5Fe-xMn alloys are labelled in the forms of TZFx.

increase from 1138 ± 34 MPa, 2.29 ± 0.06 GPa for TZF0 to 1285 ± 22 MPa, 3.78 ± 0.12 GPa for TZF2, followed by 1388 ± 22 MPa, 4.17 ± 0.13 GPa for TZF4, 1485 ± 18 MPa, 4.38 ± 0.14 GPa for TZF6 and 1580 ± 24 MPa, 4.62 ± 0.14 GPa for TZF8 respectively as the concentration of Mn increases and the grain size decreases (Table 1). This demonstrates that the effects of solid-solution strengthening according to Hume-Rothery principle [17,48] and fine-grain strengthening according to Hall-Petch empirical relationship [49–51] are liable for the rise in the values of $\sigma_{0.2}$ and hardness. The solid-solution strengthening effect ensues in the present work due to varying the content of Mn which is a low atomic radius element as compared to Ti and Zr in the investigated alloy compositions [17]. Dislocations generally require higher stresses to pass through a solute field because solute field acts as pinning points and therefore solute field exerts a resistive force on dislocations [52]. Based on this phenomenon, Fleischer reported that $\sigma_{0.2}$ is proportional to $(\text{Concentration of the solute atoms})^{2/3}$ [52].

Fig. 6 presents the plastic deformation behavior of the Ti-35Zr-5Fe-xMn alloys in terms of plastic strain. It has been observed that the values of plastic strain are immensely influenced by $V_{f,\,C14}$ and lamellar spacing (Table 1) present in the eutectic Laves matrices, therefore plastic strain decreases sharply as the values of $V_{f,\,C14}$ [53] and lamellar spacing (for the alloys comprising eutectic matrices) [1,54] increase in the present work. As a result, the highest level of plastic deformation occurs in TZF0 (23.2 ± 1.5 %) because it possesses a rod-shaped Laves phase instead of eutectic matrices, with the lowest value of $V_{f,\,C14}$ among all the as-cast alloys [2]. The plastic deformation abilities of TZF0 and

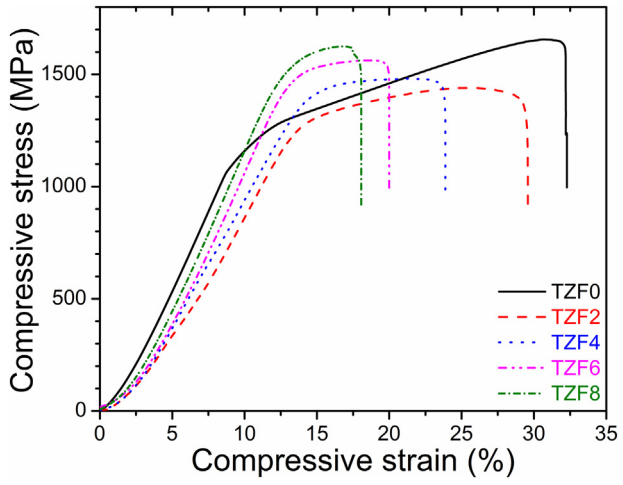

Fig. 4. The engineering stress vs. strain curves obtained from uniaxial compressive testing for the Ti-35Zr-5Fe-xMn alloys. Note that all the Ti-35Zr-5Fe-xMn alloys are labelled in the forms of TZFx.

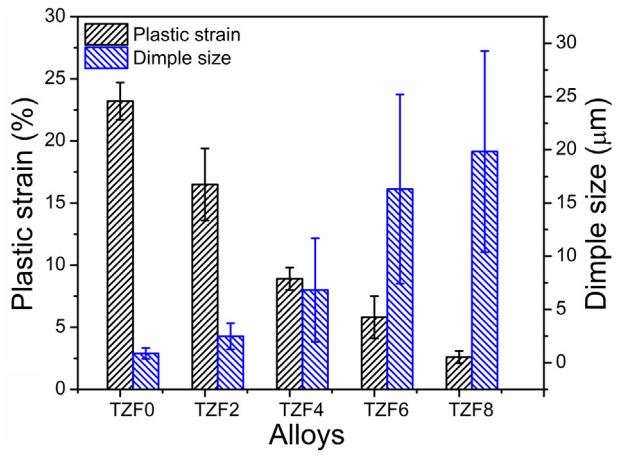

Fig. 6. The correlation between plastic strain and dimple size for the Ti-35Zr-5Fe-xMn alloys. Note that all the Ti-35Zr-5Fe-xMn alloys are labelled in the forms of TZFx.

Table 3
The comparison of the mechanical properties of the C14 and C15 type Laves phase alloys selected based on their phase and $V_{f,\ Laves}$. Note that all the Ti-35Zr-5Fe-xMn alloys are labelled in the forms of TZFx.

Alloys	Type of Laves phase	$\sigma_{0.2}$ (MPa)	σ_{max} (MPa)	Plastic strain (%)	$V_{f,\ Laves}$ (%)	Ref.
Ti-33Zr-5Fe-2Cr	C15	1128 ± 13	1830 ± 56	24.8 ± 2.5	0.8	[2]
TZF2 (Ti-35Zr-5Fe-2Mn)	C14	1285 ± 22	1498 ± 46	16.5 ± 2.9	0.9	Present work
Ti-33Zr-5Fe-4Cr	C15	1210 ± 10	1711 ± 34	22.0 ± 0.5	1.5	[2]
TZF4 (Ti-35Zr-5Fe-4Mn)	C14	1388 ± 22	1501 ± 25	8.9 ± 0.9	2.6	Present work

TZF2 based on their values of plastic strain are better than those for the previously reported Laves phase alloys [1,55,56]. In contrast, the lowest level of plastic deformation occurs in TZF8 (2.6 ± 0.5 %) because it possesses the widest lamellar spacing (1091 ± 508 nm) along with the maximum value of $V_{f,\ C14}$ among the alloys comprising eutectic matrices in the present work.

The most popular empirical relationship between $\sigma_{0.2}$ and hardness for metallic materials is $H/\sigma_{0.2} \approx 3$, where H is hardness and $\sigma_{0.2}$ is yield strength [47,57]. The values of $H/\sigma_{0.2}$ are calculated for all the investigated alloys, i.e. 2.01 for TZF0, 2.94 for TZF2, 3.0 for TZF4, 2.95 for TZF6 and 2.92 for TZF8. Zhang et al. reported the values of $H/\sigma_{0.2}$ for several ductile and brittle crystalline materials and deduced that $H/\sigma_{0.2}$ remains >3.8 for the brittle bulk metallic glasses and the ceramic materials due to possessing quite higher hardness than $\sigma_{0.2}$, whereas $H/\sigma_{0.2}$ remains <3.7 for the work-hardened ductile materials [47]. In the present work, $H/\sigma_{0.2}$ for TZF0 is 2.01 which is significantly <3.7, therefore it displays the maximum value of plastic strain among all the investigated alloys. Considering σ_{max} and plasticity, the value of $H/\sigma_{0.2}$ of TZF0 (2.01) seems optimal among all the Ti-35Zr-5Fe-xMn alloys and the value of $H/\sigma_{0.2}$ of TZF2 (2.94) seems optimal among all the alloys comprising the concentration of Mn for several structural applications.

It is always interesting to compare the mechanical properties of C14 and C15 type Laves phase alloys. Hence, two alloys comprising C15 type Laves phase, i.e. Ti-33Zr-5Fe-2Cr and Ti-33Zr-5Fe-4Cr have been chosen from our previous work [2] to compare their compressive mechanical properties with those of the TZF2 and TZF4 alloys from the present work. The other reasons to select the Ti-33Zr-5Fe-2Cr and Ti-33Zr-5Fe-4Cr alloys are: (i) these alloys comprise same or almost same

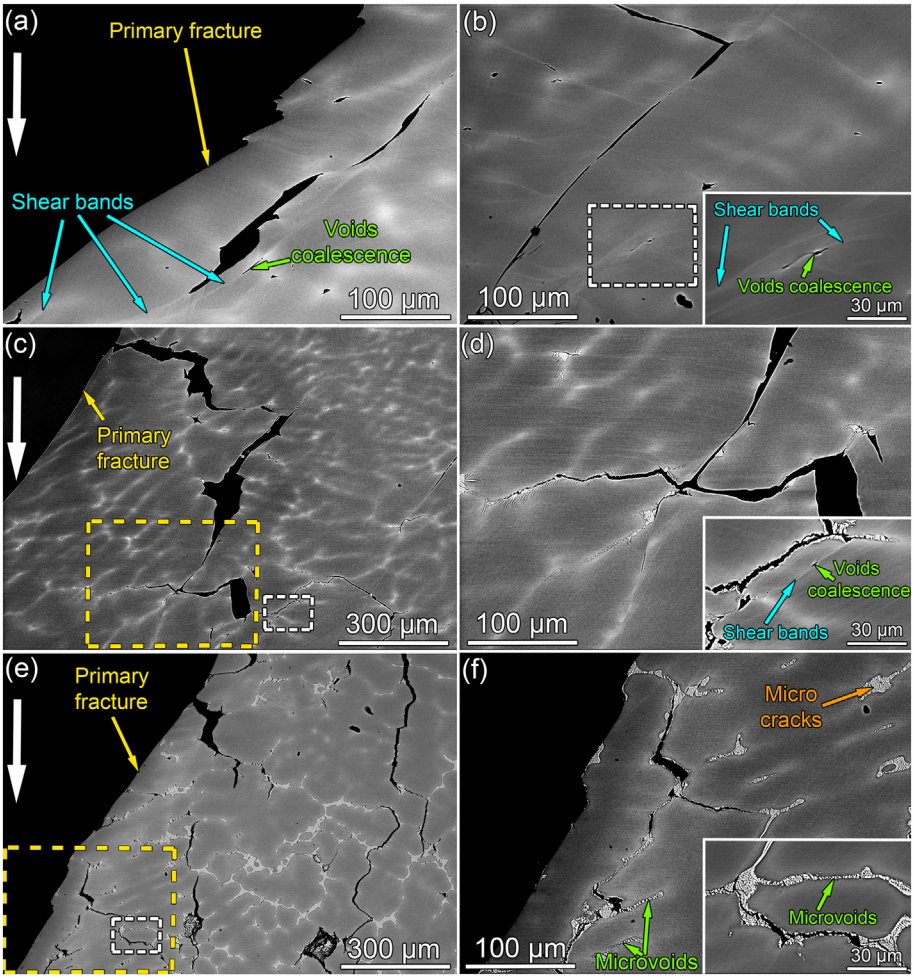

Fig. 7. The backscattered SEM images of metallographically-prepared fractured surface morphologies of (a) TZF0, (c) TZF2 and (e) TZF4. (d) and (f) are high-magnification images of the areas selected using yellow-dashed rectangles in (c) and (e) respectively. (b) is the image of TZF0 from the fractured surface area selected other than the area shown in (a). The inset images in (b), (d) and (f) are high-magnification images of the area selected using white-dashed rectangles shown in (b), (c) and (e) respectively. The downward arrows in (a), (c) and (e) specify the compression direction. Note that all the Ti-35Zr-5Fe-xMn alloys are labelled in the forms of TZFx.

contents of Fe and Zr, (ii) the concentrations of Cr are 2 wt% and 4 wt% in these respective selected alloys and these concentrations are same as those of Mn in TZF2 and TZF4 and (iii) The respective values of $V_{f,\ Laves}$ for the C14 and C15 type alloys used for the comparison in Table 3 are almost same. Thus, the mechanical properties of Ti-33Zr-5Fe-2Cr (C15 type) can be compared with TZF2 (C14 type) and Ti-33Zr-5Fe-4Cr (C15 type) can be compared with TZF4 (C14 type) based on the points discussed above. It is apparent from the comparison of the mechanical properties presented for the selected alloys in Table 3 that the C14 type Laves alloys display higher $\sigma_{0.2}$ than the C15 type Laves phase alloys, nonetheless the C15 type alloys exhibit improved plastic strain and σ_{max} than the C14 type alloys. This means that the work-hardening ability of C15 type Laves alloys is better than that of C14 type Laves alloys.

3.3. Fracture analyses

Fracture surfaces of metallic materials often retain the evidences of deformation process and failure mechanism [58]. Therefore, fracture analyses were carried out to get information about the causes of the failure occurred in the present work, which is a seminal analysis for structural metallic materials. Fig. 7 and Fig. 8 display the backscattered SEM images of metallographically prepared fractured surface morphologies of all the investigated alloys along with their respective high-magnification images. The primary shearing fracture lines of all the Ti-35Zr-5Fe-xMn alloys are displayed in Fig. 7 and Fig. 8. Furthermore, TZF0 exhibits many long shear bands, while only few shear bands are seen in the alloys comprising the content of Mn in the present work. Shear bands usually form due to localized plastic flow generated as a result of plastic instability [59]. TZF0 contains a greater number of shear bands among all the Ti-35Zr-5Fe-xMn alloys, therefore TZF0 shows the maximum plastic deformation in this work. Other than this, micro-voids and coalescence of micro-voids are found in the fracture morphologies of TZF0, TZF2, TZF4 and TZF6. There are three fundamental stages of crack development: (i) nucleation of voids, (ii) growth of voids and (iii) coalescence of voids [60]. The cracks usually develop after undergoing above three stages along the high stress concentrated regions such as shear bands and second phase particles [60]. In the present work, the coalescences of voids over the shear bands are clearly seen in Fig. 7 and Fig. 8. A crack usually propagates further from the void coalescences if more stress is applied on the void coalescences. The propagation of secondary cracks along the shear bands is found in TZF0 (Fig. 7a and b) because TZF0 comprises maximum value of $V_{f,\ \beta}$ among all the as-cast alloys. This implies that the primary fracture should have occurred in a transgranular mode along the main thick shear band in TZF0. On the other hand, the propagation of secondary cracks mainly occur along the brittle Laves phase in TZF2, TZF4, TZF6 and TZF8. This suggests that the primary fracture occurs in an intergranular mode through the eutectic matrices formed over the grain boundaries in TZF2, TZF4, TZF6 and TZF8 as shown in Fig. 7 and Fig. 8. Significantly, it has been noticed in the fracture morphologies of the alloys comprising the content of Mn that the secondary cracks are unable to cross over the Laves matrix to the β matrix but deflected along the eutectic Laves matrices. This means that β matrix possesses high fracture toughness as compared to Laves phase.

The shear bands displayed in Fig. 7 and Fig. 8 form over the β matrix because β matrix is very much softer than the hard Laves matrix. As a result, the shear bands are not found in TZF8 because it comprises the maximum value of $V_{f,\ C14}$. It has also been observed in Fig. 7d inset that Laves phase impedes the propagation of shear bands. Shear bands are unable to pass through the hard Laves matrix. This means that a higher stress is required for dislocation motions to pass through the Laves phase matrix and Laves matrix also exerts a high resistive force on dislocations due to having a special topologically closed-packed structure [1]. As a result, the Laves matrix becomes a high stress concentrated region, which leads to the failure of the brittle Laves matrix prior to the soft β matrix. Consequently, micro-cracks and micro-voids also form inside the high stress concentrated separate Laves matrices other than the Laves matrices where secondary cracks are already developed in the TZF4 (Fig. 7f), TZF6 (Fig. 8b) and TZF8 (Fig. 8d) alloys.

The fracture energy generally consists of elastic and plastic energies [61]. The stored elastic energy usually dissipate in doing plastic deformation and or developing cracks [2]. The elastic energy in ductile materials is dissipated more in doing plastic deformation due to having high

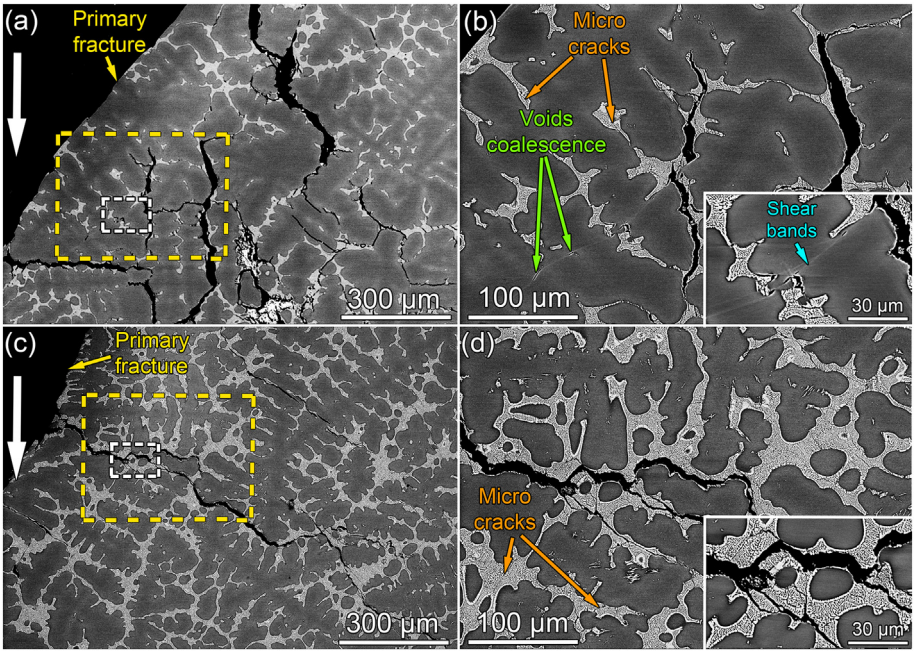

Fig. 8. The backscattered SEM images of metallographically-prepared fractured surface morphologies of (a) TZF6 and (c) TZF8. (b) and (d) are high-magnification images of the areas selected using yellow-dashed rectangles in (a) and (c) respectively. The inset images in (b) and (d) are high-magnification images of the area selected using white-dashed rectangles in (a) and (c) respectively. The downward arrows in (a) and (c) specify the compression direction. Note that all the Ti-35Zr-5Fe-xMn alloys are labelled in the forms of TZFx.

fracture toughness, whereas the elastic energy in brittle materials is dissipated in the form of heat in developing cracks because the elastic energy absorption capacity of a brittle material is less than that of a ductile material [2]. The elastic energy is directly proportional to yield strength of a material [19]. In the present work, TZF0 demonstrated the lowest yield strength (1138 ± 34 MPa) value, whereas TZF8 demonstrated the maximum yield strength (1580 ± 24 MPa) value as discussed earlier. This means that TZF8 should have higher elastic energy than TZF0 in the present work. Thus, a higher amount of elastic energy should have been stored in TZF8 than that stored in TZF0 during the deformation process, but TZF8 comprises the maximum $V_{f,\,C14}$ in the present work and the Laves matrix possesses poor elastic energy absorption capacity. Consequently, TZF8 failed early after showing plastic strain of only 2.6 ± 0.5 %.

In addition, the fracture angles were measured from the compression direction using low magnification images in ImageJ software for all the investigated alloys. The average values of fracture angle are 39 ± 0.8°, 43.9 ± 0.7°, 42.4 ± 0.6°, 43.5 ± 0.9° and 39.2 ± 1.8° for TZF0, TZF2, TZF4, TZF6 and TZF8 respectively. The primary fractures in the investigated alloys occurred at <45° angles, which indicate that all the alloys analyzed in this work failed according to the Mohr-Coulomb failure principle (in which both normal and shear stress components remain responsible for a failure) instead of the Von-Mises failure principle (in which only shear stress components remain responsible for a failure) [60,62].

The SEM fractographic images (in secondary electron mode) are also captured and illustrated in Fig. 9 for all the Ti-35Zr-5Fe-xMn alloys. The dimple morphologies are found on fractured surfaces of all the investigated alloys (Fig. 9). The inset images in Fig. 9 present the magnified view of the dimples. Dimple features often result from the plastic instabilities, therefore dimple features are indicative of a level of plastic deformation [63]. The size, the shape and the number of dimples are not dependent on the grain size, but depend on the type of loading, the size and the amount of the microstructural phases [63,64]. Consequently, the maximum dimple density (i.e. the number of dimples in a specified area) is found in TZF0 because it shows the maximum level of plastic deformation among all the as-cast alloys. It is evident in Fig. 9 that as the value of $V_{f,\,C14}$ increases in the present work, the dimple density reduces and cleavage features are more dominant.

Additionally, the size of the dimples was also measured using ImageJ software for all the as-cast alloys. The average dimple sizes of TZF0, TZF2, TZF4, TZF6 and TZF8 are 0.87 ± 0.50 μm, 2.48 ± 1.22 μm, 6.83 ± 4.87 μm, 16.31 ± 8.90 μm and 19.82 ± 9.45 μm respectively. The inverse correlation between dimple size and plastic strain for all the Ti-35Zr-5Fe-xMn alloys is evident in Fig. 6 which reveals that the dimple size increases as plastic strain decreases in the present work. Moreover, it is also fascinating to observe the brittle fracture that occurred along the grain boundaries in the fractographic image of TZF8 (Fig. 9f). The feature of the fracture shown in Fig. 9f is another evidence of intergranular fracture happened in TZF8.

In the present work, the evidences of the correlation between the results of the microstructure and the results of the mechanical properties and the fracture analyses can be summarized as: (i) $\sigma_{0.2}$ and hardness increase as $V_{f,\,C14}$ increases. (ii) The values of plastic strain and

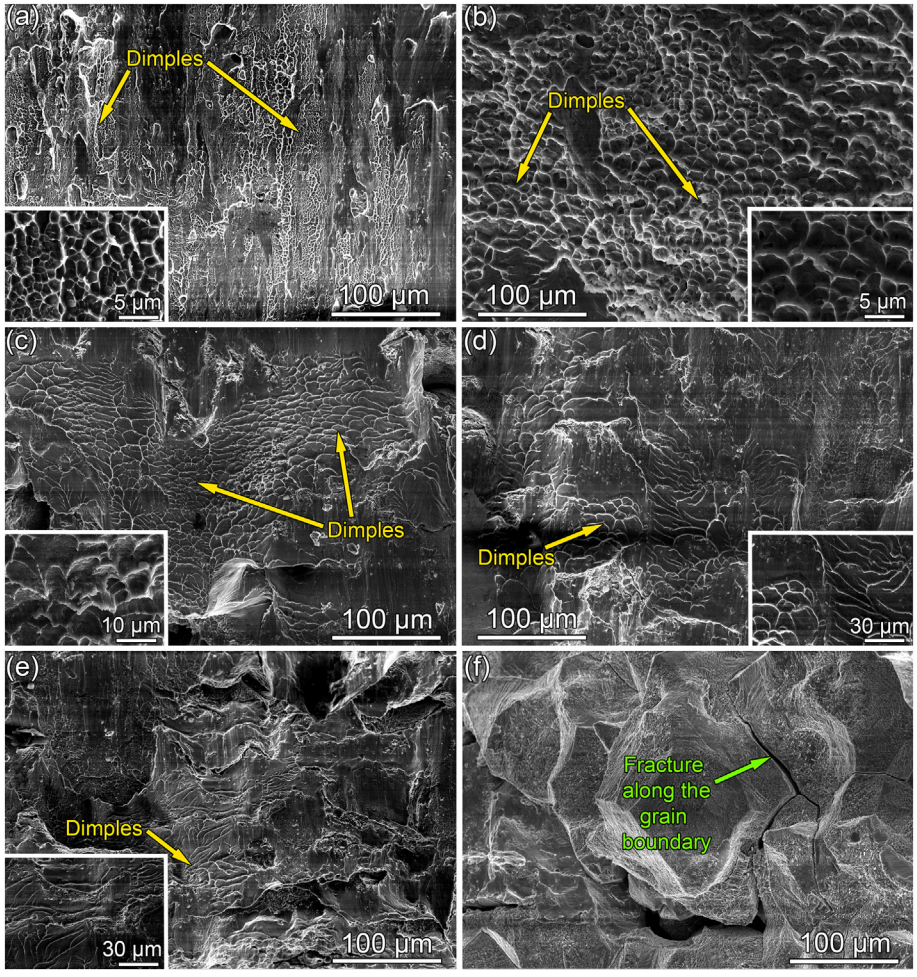

Fig. 9. The SEM fractographic images of (a) TZF0, (b) TZF2, (c) TZF4, (d) TZF6, (e) and (f) TZF8. The inset images in (a)–(e) show high-magnification images taken for the respective alloys. Note that all the Ti-35Zr-5Fe-xMn alloys are labelled in the forms of TZFx.

elongation decrease as $V_{f,\,C14}$ increases. (iii) The values of σ_{max} are influenced by the type of a Laves phase, morphology of the Laves phase and the corresponding V_f of the Laves phase. (iv) Due to comprising the highest value of $V_{f,\,\beta}$, TZF0 fails in a transgranular mode and shows the maximum number of several long shear bands, the maximum dimple density and the maximum level of plastic deformation. (v) The alloys comprising eutectic morphologies in the microstructure (TZF2, TZF4, TZF6 and TZF8) fail in an intergranular mode. (vi) The plastic deformation ability of the alloys comprising eutectic morphologies in the microstructure decreases as the value of $V_{f,\,14}$ increases. Based on the points discussed above, it can be inferred that the results of the microstructure analyses are evidently in line with the results of the mechanical properties and fracture analyses.

3.4. Elasto-plastic behavior around the micro-hardness indentations

The investigation of elasto-plastic behavior around the micro and nano-hardness indentations become widely popular because these techniques are relatively simple as compared to conventional methods. In hardness testing, when hardness indenter penetrates on the surface of the material, elastic and plastic deformations occur underneath and around the hardness indenter [65,66]. As a result, several patterns of slip bands and or cracks form around the hardness indentation depending on the toughness and work hardening ability of materials [47,67]. The slip bands around the hardness indentation are indicative of plastic deformation, whereas the cracks around the hardness indentation are indicative of brittle and relatively less tough nature of a material. During the indentation process, the material near the edges deforms by normal as well as shear stress components and the material near the corners deforms only by normal stress components [47].

Fig. 10 depicts the patterns of the slip bands observed around the hardness indentation of all the Ti-35Zr-5Fe-xMn alloys along with the illustration of high-magnification images shown in the respective inset images. Previous studies show that there is a direct relationship between the work-hardening ability of a material and the density of slip bands (i.e. number of slip bands in a specified area) around the hardness indentations [47]. Consequently, the maximum density of slip bands is found in TZF0 (Fig. 10a) because it possesses the maximum value of plastic strain among all the as-cast alloys. The density of slip bands then decreases as the values of plastic strain decrease in alloys comprising the content of Mn.

In addition, three small-cracks can be observed at the corners of the indentation employed for TZF8 (Inset image of Fig. 10e). The cracks around the hardness indentation mostly form in brittle materials and the average length of a crack remains inversely proportional to fracture toughness of materials [67,68]. This phenomenon reveals the poor fracture toughness of TZF8 as compared to other investigated alloys. It is also worth noting that the investigation results of elasto-plastic behavior obtained around the micro-hardness indentations for all the investigated alloys are undoubtedly in line with those of the microstructure and mechanical properties.

4. Conclusion

The evaluations of microstructure, mechanical properties, fracture behavior and the elasto-plastic behavior analyzed around the micro-

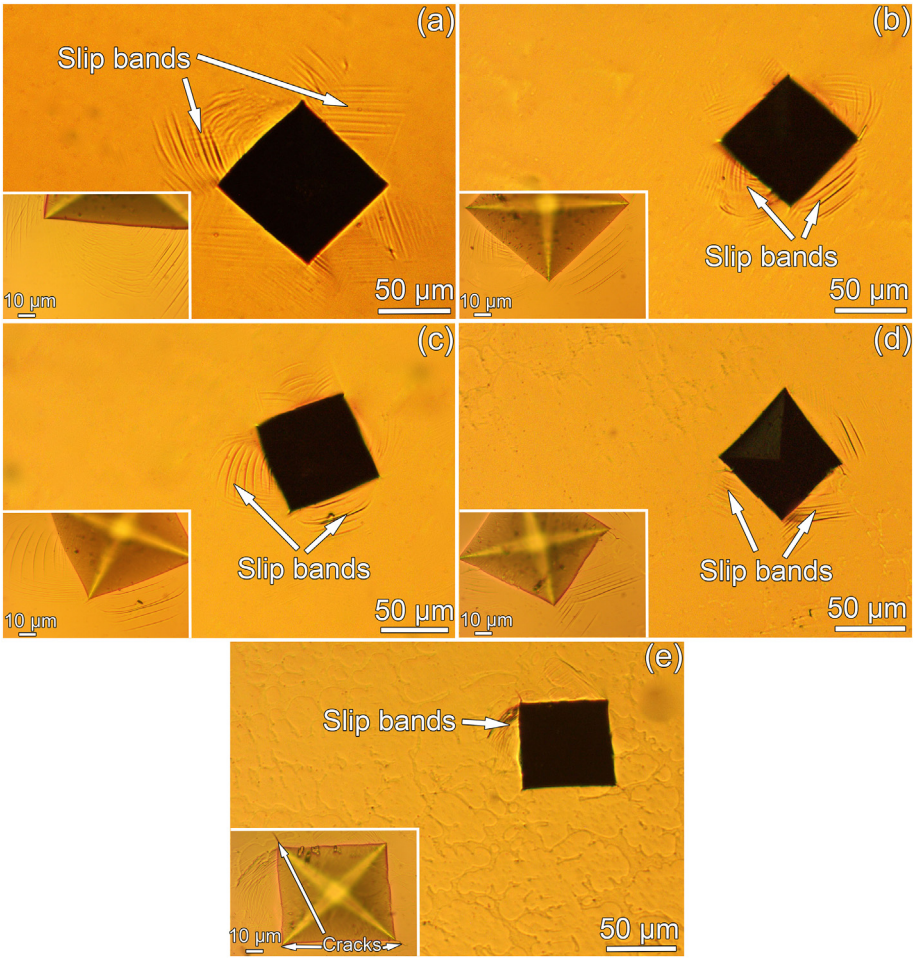

Fig. 10. The optical morphologies obtained around the micro-hardness indentions of (a) TZF0, (b) TZF2, (c) TZF4, (d) TZF6 and (e) TZF8. The inset images in (a)–(e) show high-magnification images taken for the respective alloys. Note that all the Ti-35Zr-5Fe-xMn alloys are labelled in the forms of TZFx.

hardness indentation are employed for the as-cast Ti-35Zr-5Fe-xMn (x = 0, 2, 4, 6, 8 wt%) alloys. The key concluding remarks of this work are outlined below.

- A C14 type Laves phase and a dominating bcc β phase are identified in all the as-cast alloys based on the XRD, SEM and EDX analyses. The present work also demonstrates that the concentration of Mn is very sensitive to raise the volume fraction of Laves phase in the as-cast alloys.
- Yield strength and hardness of the investigated alloys are affected by solid-solution strengthening and fine-grain strengthening. The values of plastic strain are considerably affected by volume fraction of the Laves phase and lamellar spacing present in the eutectic matrices.
- Ti-35Zr-5Fe demonstrates enhanced mechanical properties, including superior ultimate compressive strength (~1.7 GPa), high yield strength (1138 MPa), high hardness (2.29 GPa) and large plastic strain (23.2 %). Ti-35Zr-5Fe also possesses the lowest hardness to yield strength ratio (2.01) which indicates an improved work-hardening ability in this alloy. The Ti-35Zr-5Fe alloy is promising alloy for several automotive and aerospace applications considering its impressive attributes.
- The C15 type alloys display a large plastic strain than those of the C14 type alloys based on the comparison of the mechanical properties of the selected C14 and C15 type Laves phase alloys.
- The fracture analyses reveal that Ti-35Zr-5Fe fails in a transgranular mode, whereas the remaining alloys fail in an intergranular mode. The fracture analyses also demonstrate that shear bands easily form over the soft microstructure matrix as compared to hard microstructure matrix. The inverse correlation between dimple size and the plastic deformation ability is obtained for all the as-cast alloys.
- The formation of slip bands around the hardness indentation is influenced by the work-hardening ability of the as-cast alloys.
- The results of microstructure, mechanical properties, failure analyses, elasto-plastic behavior analyzed around the hardness indentations for all the investigated alloys are interrelated with each other.
- Importantly, all the Ti-35Zr-5Fe-xMn alloys do not fail within the elastic limit and all demonstrate the improved compressive elongation values, including the maximum (32.5 %) in Ti-35Zr-5Fe.

Author contributions

C.D.R and L.C.Z. conceived the experiments, analyzed the data and wrote the manuscript. C.D.R., Y.J.L., S.F.J. and L.W. conducted the experiments. All authors discussed the results and reviewed the manuscript.

Acknowledgement

The authors would like to acknowledge the financial supports provided by National Science Foundation of China under Grant No. 51674167 and Fundamental Research Funds for the Central Universities in China under Grant No. YG2017ZD06.

References

[1] S. Scudino, P. Donnadieu, K.B. Surreddi, K. Nikolowski, M. Stoica, J. Eckert, Microstructure and mechanical properties of Laves phase-reinforced Fe-Zr-Cr alloys, Intermetallics 17 (2009) 532–539, https://doi.org/10.1016/j.intermet.2009.01.007.
[2] C.D. Rabadia, Y.J. Liu, L. Wang, H. Sun, L.C. Zhang, Laves phase precipitation in Ti-Zr-Fe-Cr alloys with high strength and large plasticity, Mater. Des. 154 (2018) 228–238, https://doi.org/10.1016/j.matdes.2018.05.035.
[3] F. Chu, D.J. Thoma, P.G. Kotula, S. Gerstl, T.E. Mitchell, I.M. Anderson, J. Bentley, Phase stability and defect structure of the C15 Laves phase $Nb(Cr,V)_2$, Acta Mater. 46 (1998) 1759–1769, https://doi.org/10.1016/S1359-6454(97)00291-7.
[4] F. Stein, M. Palm, G. Sauthoff, Structure and stability of Laves phases. Part I. Critical assessment of factors controlling Laves phase stability, Intermetallics 12 (2004) 713–720, https://doi.org/10.1016/j.intermet.2004.02.010.
[5] W. Luo, C. Kirchlechner, X. Fang, S. Brinckmann, G. Dehm, F. Stein, Influence of composition and crystal structure on the fracture toughness of $NbCo_2$ Laves phase studied by micro-cantilever bending tests, Mater. Des. 145 (2018) 116–121, https://doi.org/10.1016/j.matdes.2018.02.045.
[6] W. Huo, H. Zhou, F. Fang, Z. Xie, J. Jiang, Microstructure and mechanical properties of $CoCrFeNiZr_x$ eutectic high-entropy alloys, Mater. Des. 134 (2017) 226–233, https://doi.org/10.1016/j.matdes.2017.08.030.
[7] X.Y. Meng, D. Northwood, Polytype structures in Zr-Cr-Fe laves phase, J. Less-Common Met. 125 (1986) 33–44, https://doi.org/10.1016/0022-5088(86)90078-0.
[8] J. Huot, E. Akiba, Y. Ishido, Crystal structure of multiphase alloys $(Zr, Ti)(Mn, V)_2$, J. Alloys Compd. 231 (1995) 85–89, https://doi.org/10.1016/0925-8388(95)01842-5.
[9] D.J. Thoma, J.H. Perepezko, A geometric analysis of solubility ranges in Laves phases, J. Alloys Compd. 224 (1995) 330–341, https://doi.org/10.1016/0925-8388(95)01557-4.
[10] J. Nei, K. Young, S.O. Salley, K.Y.S. Ng, Determination of C14/C15 phase abundance in Laves phase alloys, Mater. Chem. Phys. 136 (2012) 520–527, https://doi.org/10.1016/j.matchemphys.2012.07.020.
[11] A.J. Knowles, A. Bhowmik, S. Purkayastha, N.G. Jones, F. Giuliani, W.J. Clegg, D. Dye, H.J. Stone, Laves phase intermetallic matrix composite in situ toughened by ductile precipitates, Scr. Mater. 140 (2017) 59–62, https://doi.org/10.1016/j.scriptamat.2017.06.043.
[12] L. Zhang, J. Das, H. Lu, C. Duhamel, M. Calin, J. Eckert, High strength Ti–Fe–Sn ultrafine composites with large plasticity, Scr. Mater. 57 (2007) 101–104, https://doi.org/10.1016/j.scriptamat.2007.03.031.
[13] L. Wang, L. Xie, Y. Lv, L. Zhang, L. Chen, Q. Meng, J. Qu, D. Zhang, W. Lu, Microstructure evolution and superelastic behavior in Ti-35Nb-2Ta-3Zr alloy processed by friction stir processing, Acta Mater. 131 (2017) 499–510, https://doi.org/10.1016/j.actamat.2017.03.079.
[14] P. Qin, Y. Liu, T.B. Sercombe, Y. Li, C. Zhang, C. Cao, H. Sun, L.C. Zhang, Improved corrosion resistance on selective laser melting produced Ti-5Cu alloy after heat treatment, ACS Biomater. Sci. Eng. 4 (2018) 2633–2642, https://doi.org/10.1021/acsbiomaterials.8b00319.
[15] Y.J. Liu, H.L. Wang, S.J. Li, S.G. Wang, W.J. Wang, W.T. Hou, Y.L. Hao, R. Yang, L.C. Zhang, Compressive and fatigue behavior of beta-type titanium porous structures fabricated by electron beam melting, Acta Mater. 126 (2017) 58–66, https://doi.org/10.1016/j.actamat.2016.12.052.
[16] S. Huang, X. Zhang, Y. Jiang, Y. Jiang, C. Mao, D. Wu, L. Zhang, L. Liu, Experimental investigation of Ti-Nb-Co ternary system at 1000 °C, Mater. Des. 115 (2017) 170–178, https://doi.org/10.1016/j.matdes.2016.11.056.
[17] C. Liu, J.Q. Qin, Z.H. Feng, S.L. Zhang, M.Z. Ma, X.Y. Zhang, R.P. Liu, Improving the microstructure and mechanical properties of Zr-Ti alloy by nickel addition, J. Alloys Compd. 737 (2018) 405–411, https://doi.org/10.1016/j.jallcom.2017.12.046.
[18] S. Ehtemam-Haghighi, K.G. Prashanth, H. Attar, A.K. Chaubey, G.H. Cao, L.C. Zhang, Evaluation of mechanical and wear properties of TixNb7Fe alloys designed for biomedical applications, Mater. Des. 111 (2016) 592–599, https://doi.org/10.1016/j.matdes.2016.09.029.
[19] S. Ehtemam-Haghighi, Y. Liu, G. Cao, L.C. Zhang, Phase transition, microstructural evolution and mechanical properties of Ti-Nb-Fe alloys induced by Fe addition, Mater. Des. 97 (2016) 279–286, https://doi.org/10.1016/j.matdes.2016.02.094.
[20] S. Ehtemam-Haghighi, H.B. Lu, G.Y. Jian, G.H. Cao, D. Habibi, L.C. Zhang, Effect of α″ martensite on the microstructure and mechanical properties of beta-type Ti–Fe–Ta alloys, Mater. Des. 76 (2015) 47–54, https://doi.org/10.1016/j.matdes.2015.03.028.
[21] R.P. Kolli, A. Devaraj, A review of metastable beta titanium alloys, Metals 8 (2018) 506, https://doi.org/10.3390/met8070506.
[22] C.D. Rabadia, Y.J. Liu, G.H. Cao, Y.H. Li, C.W. Zhang, T.B. Sercombe, H. Sun, L.C. Zhang, High-strength β stabilized Ti-Nb-Fe-Cr alloys with large plasticity, Mater. Sci. Eng. A 732 (2018) 368–377, https://doi.org/10.1016/j.msea.2018.07.031.
[23] Y.D. Shi, L.N. Wang, S.X. Liang, Q. Zhou, B. Zheng, A high Zr-containing Ti-based alloy with ultralow Young's modulus and ultrahigh strength and elastic admissible strain, Mater. Sci. Eng. A 674 (2016) 696–700, https://doi.org/10.1016/j.msea.2016.08.038.
[24] T. Ishimasa, Chapter 3 New Group of Icosahedral Quasicrystals, in: T. Fujiwara, Y. Ishii (Eds.), Handbook of Metal Physics, Elsevier, Oxford 2008, pp. 49–74.
[25] N.N. Greenwood, A. Earnshaw, Chemistry of the Elements, second ed. Elsevier, Oxford, 2012.
[26] M.E. Schlesinger, The Mn-Zr (manganese-zirconium) system, J. Phase Equilib. 20 (1999) 79–83, https://doi.org/10.1361/105497199770335983.
[27] V. Ivanchenko, Mn-Ti-Zr (Manganese-Titanium-Zirconium), in: G. Effenberg, S. Ilyenko (Eds.), Non-Ferrous Metal Systems. Part 3: Selected Soldering and Brazing Systems, Springer Berlin Heidelberg, Berlin, Heidelberg 2007, pp. 475–485.
[28] V. Raghavan, Fe-Ti-Zr (Iron-Titanium-Zirconium), J. Phase Equilib. 31 (2010) 469, https://doi.org/10.1007/s11669-010-9751-3.
[29] X. Jin, S. Chen, L. Rong, Effect of Fe_2Zr phase on the mechanical properties and fracture behavior of Fe-Cr-W-Zr ferritic alloy, Mater. Sci. Eng. A 722 (2018) 173–181, https://doi.org/10.1016/j.msea.2018.03.033.
[30] L.C. Zhang, Z.Q. Shen, J. Xu, Glass formation in a (Ti, Zr, Hf)–(Cu, Ni, Ag)–Al high-order alloy system by mechanical alloying, J. Mater. Res. 18 (2003) 2141–2149, https://doi.org/10.1557/JMR.2003.0300.
[31] S. Ehtemam-Haghighi, G. Cao, L.C. Zhang, Nanoindentation study of mechanical properties of Ti based alloys with Fe and Ta additions, J. Alloys Compd. 692 (2017) 892–897, https://doi.org/10.1016/j.jallcom.2016.09.123.
[32] G. Li, N. Nishimiya, H. Satoh, N. Kamegashira, Crystal structure and hydrogen absorption of $Ti_xZr_{1-x}Mn_2$, J. Alloys Compd. 393 (2005) 231–238, https://doi.org/10.1016/j.jallcom.2004.08.097.
[33] H. Flandorfer, J. Grobner, A. Stamou, N. Hassiotis, A. Saccone, P. Rogl, R. Wouters, H. Seifert, D. Maccio, R. Ferro, G. Haidemenopoulos, L. Delaey, G. Effenberg, Experimental investigation and thermodynamic calculation of the ternary system Mn-Y-Zr, Z. Met. 88 (1997) 529–538.
[34] C.C. Silva, H.C. de Miranda, M.F. Motta, J.P. Farias, C.R.M. Afonso, A.J. Ramirez, New insight on the solidification path of an alloy 625 weld overlay, J. Mater. Res. Technol. 2 (2013) 228–237, https://doi.org/10.1016/j.jmrt.2013.02.008.

[35] E.L. Stevens, J. Toman, A.C. To, M. Chmielus, Variation of hardness, microstructure, and Laves phase distribution in direct laser deposited alloy 718 cuboids, Mater. Des. 119 (2017) 188–198, https://doi.org/10.1016/j.matdes.2017.01.031.
[36] Y.D. Wu, Y.H. Cai, X.H. Chen, T. Wang, J.J. Si, L. Wang, Y.D. Wang, X.D. Hui, Phase composition and solid solution strengthening effect in TiZrNbMoV high-entropy alloys, Mater. Des. 83 (2015) 651–660, https://doi.org/10.1016/j.matdes.2015.06.072.
[37] D. Aboudi, S. Lebaili, M. Taouinet, J. Zollinger, Microstructure evolution of diffusion welded 304L/Zircaloy4 with copper interlayer, Mater. Des. 116 (2017) 386–394, https://doi.org/10.1016/j.matdes.2016.12.008.
[38] F. Stein, G. Sauthoff, M. Palm, Experimental determination of intermetallic phases, phase equilibria, and invariant reaction temperatures in the Fe-Zr system, J. Phase Equilib. 23 (2002) 480, https://doi.org/10.1361/105497102770331172.
[39] G. Gottstein, Physical Foundations of Materials Science, first ed. Springer Science & Business Media, Springer-Verlag Berlin Heidelberg New York, 2013.
[40] A. Devaraj, W. Wang, R. Vemuri, L. Kovarik, X. Jiang, M. Bowden, J.R. Trelewicz, S. Mathaudhu, A. Rohatgi, Grain boundary segregation and intermetallic precipitation in coarsening resistant nanocrystalline aluminum alloys, Acta Mater. (2018)https://doi.org/10.1016/j.actamat.2018.09.038.
[41] N.Y. Yurchenko, N.D. Stepanov, A.O. Gridneva, M.V. Mishunin, G.A. Salishchev, S.V. Zherebtsov, Effect of Cr and Zr on phase stability of refractory Al-Cr-Nb-Ti-V-Zr high-entropy alloys, J. Alloys Compd. 757 (2018) 403–414, https://doi.org/10.1016/j.jallcom.2018.05.099.
[42] D.D. Risanti, G. Sauthoff, Strengthening of iron aluminide alloys by atomic ordering and laves phase precipitation for high-temperature applications, Intermetallics 13 (2005) 1313–1321, https://doi.org/10.1016/j.intermet.2004.12.029.
[43] C. Ai, F. He, M. Guo, J. Zhou, Z.J. Wang, Z.W. Yuan, Y.J. Guo, Y.L. Liu, L. Liu, Alloy design, micromechanical and macromechanical properties of $CoCrFeNiTa_x$ eutectic high entropy alloys, J. Alloys Compd. 735 (2018) 2653–2662, https://doi.org/10.1016/j.jallcom.2017.12.015.
[44] X. Li, J.J. Shi, C.H. Wang, G.H. Cao, A.M. Russell, Z.J. Zhou, C.P. Li, G.F. Chen, Effect of heat treatment on microstructure evolution of Inconel 718 alloy fabricated by selective laser melting, J. Alloys Compd. 764 (2018) 639–649, https://doi.org/10.1016/j.jallcom.2018.06.112.
[45] P. Xie, M. Han, C.L. Wu, Y.Q. Yin, K. Zhu, R.H. Shen, J.H. Chen, A high-performance TRIP steel enhanced by ultrafine grains and hardening precipitates, Mater. Des. 127 (2017) 1–7, https://doi.org/10.1016/j.matdes.2017.04.063.
[46] F.C. Campbell, Chapter 5: eutectic alloy systems, in: F.C. Campbell (Ed.), Phase Diagrams: Understanding the Basics, ASM International, Ohio, 2012.
[47] P. Zhang, S.X. Li, Z.F. Zhang, General relationship between strength and hardness, Mater. Sci. Eng. A 529 (2011) 62–73, https://doi.org/10.1016/j.msea.2011.08.061.
[48] F.G. Coury, T. Butler, K. Chaput, A. Saville, J. Copley, J. Foltz, P. Mason, K. Clarke, M. Kaufman, A. Clarke, Phase equilibria, mechanical properties and design of quaternary refractory high entropy alloys, Mater. Des. 155 (2018) 244–256, https://doi.org/10.1016/j.matdes.2018.06.003.
[49] B. Gwalani, V. Soni, M. Lee, S.A. Mantri, Y. Ren, R. Banerjee, Optimizing the coupled effects of Hall-Petch and precipitation strengthening in a $Al_{0.3}CoCrFeNi$ high entropy alloy, Mater. Des. 121 (2017) 254–260, https://doi.org/10.1016/j.matdes.2017.02.072.
[50] L.C. Zhang, Y. Liu, S. Li, Y. Hao, Additive manufacturing of titanium alloys by electron beam melting: a review, Adv. Eng. Mater. 20 (2018), 1700842. https://doi.org/10.1002/adem.201700842.
[51] L.Y. Du, L. Wang, W. Zhai, L. Hu, J.M. Liu, B. Wei, Liquid state property, structural evolution and mechanical behavior of TiFe alloy solidified under electrostatic levitation condition, Mater. Des. 160 (2018) 48–57, https://doi.org/10.1016/j.matdes.2018.08.043.
[52] R.L. Fleisgher, Solution hardening, Acta Metall. 9 (1961) 996–1000, https://doi.org/10.1016/0001-6160(61)90242-5.
[53] L.H. Liu, C. Yang, F. Wang, S.G. Qu, X.Q. Li, W.W. Zhang, Y.Y. Li, L.C. Zhang, Ultrafine grained Ti-based composites with ultrahigh strength and ductility achieved by equiaxing microstructure, Mater. Des. 79 (2015) 1–5, https://doi.org/10.1016/j.matdes.2015.04.032.
[54] L.Y. Sheng, J.T. Guo, H.Q. Ye, Microstructure and mechanical properties of NiAl–Cr (Mo)/Nb eutectic alloy prepared by injection-casting, Mater. Des. 30 (2009) 964–969, https://doi.org/10.1016/j.matdes.2008.06.061.
[55] P. Donnadieu, C. Pohlmann, S. Scudino, J.J. Blandin, K.B. Surreddi, J. Eckert, Deformation at ambient and high temperature of in situ laves phases-ferrite composites, Sci. Technol. Adv. Mater. 15 (2014), 034801. https://doi.org/10.1088/1468-6996/15/3/034801.
[56] M. Takeyama, C.T. Liu, Microstructure and mechanical-properties of laves-phase alloys based on Cr_2Nb, Mater. Sci. Eng. A 132 (1991) 61–66, https://doi.org/10.1016/0921-5093(91)90361-P.
[57] A. Ruiz-Moreno, P. Hähner, Indentation size effects of ferritic/martensitic steels: a comparative experimental and modelling study, Mater. Des. 145 (2018) 168–180, https://doi.org/10.1016/j.matdes.2018.02.064.
[58] A. Das, S. Tarafder, Geometry of dimples and its correlation with mechanical properties in austenitic stainless steel, Scr. Mater. 59 (2008) 1014–1017, https://doi.org/10.1016/j.scriptamat.2008.07.012.
[59] J.L. Sun, P.W. Trimby, F.K. Yan, X.Z. Liao, N.R. Tao, J.T. Wang, Shear banding in commercial pure titanium deformed by dynamic compression, Acta Mater. 79 (2014) 47–58, https://doi.org/10.1016/j.actamat.2014.07.011.
[60] B.A. Sun, W.H. Wang, The fracture of bulk metallic glasses, Prog. Mater. Sci. 74 (2015) 211–307, https://doi.org/10.1016/j.pmatsci.2015.05.002.
[61] Y.J. Liu, S.J. Li, L.C. Zhang, Y.L. Hao, T.B. Sercombe, Early plastic deformation behaviour and energy absorption in porous β-type biomedical titanium produced by selective laser melting, Scr. Mater. 153 (2018) 99–103, https://doi.org/10.1016/j.scriptamat.2018.05.010.
[62] R. Vaidyanathan, M. Dao, G. Ravichandran, S. Suresh, Study of mechanical deformation in bulk metallic glass through instrumented indentation, Acta Mater. 49 (2001) 3781–3789, https://doi.org/10.1016/S1359-6454(01)00263-4.
[63] A. Hasnaoui, H. Van Swygenhoven, P.M. Derlet, Dimples on nanocrystalline fracture surfaces as evidence for shear plane formation, Science 300 (2003) 1550–1552, https://doi.org/10.1126/science.1084284.
[64] J. Fan, J. Li, H. Kou, K. Hua, B. Tang, Y. Zhang, Microstructure and mechanical property correlation and property optimization of a near β titanium alloy Ti-7333, J. Alloys Compd. 682 (2016) 517–524, https://doi.org/10.1016/j.jallcom.2016.04.303.
[65] U. Ramamurty, S. Jana, Y. Kawamura, K. Chattopadhyay, Hardness and plastic deformation in a bulk metallic glass, Acta Mater. 53 (2005) 705–717, https://doi.org/10.1016/j.actamat.2004.10.023.
[66] S. Ehtemam-Haghighi, Y. Liu, G. Cao, L.C. Zhang, Influence of Nb on the $\beta \rightarrow \alpha''$ martensitic phase transformation and properties of the newly designed Ti-Fe-Nb alloys, Mater. Sci. Eng. C 60 (2016) 503–510, https://doi.org/10.1016/j.msec.2015.11.072.
[67] P. Sellappan, T. Rouxel, F. Celarie, E. Becker, P. Houizot, R. Conradt, Composition dependence of indentation deformation and indentation cracking in glass, Acta Mater. 61 (2013) 5949–5965, https://doi.org/10.1016/j.actamat.2013.06.034.
[68] D. Ćorić, M. Majić Renjo, L. Čurković, Vickers indentation fracture toughness of Y-TZP dental ceramics, Int. J. Refract. Met. Hard Mater. 64 (2017) 14–19, https://doi.org/10.1016/j.ijrmhm.2016.12.016.